Numerical Simulations of Rotors Using High Fidelity Methods

A. Jimenez-Garcia[a], G.N. Barakos[b]
CFD Laboratory, School of Engineering, University of Glasgow, G12 8QQ Glasgow, UK

This paper presents numerical simulations of rotors using modern CFD methods. First, the performance analysis of the XV-15 tiltrotor blade is presented. Results are shown for a range of design points, which include medium and high thrust hover conditions. Then, the effect of transition on the predicted figure of merit is shown at collective angles of 3° and 10°. Hovering simulations for the PSP blade are also shown. The paper closes with simulations of the UH-60A rotor in forward flight.

Nomenclature

$\boldsymbol{R}$	=	flow equation residual vector
$\boldsymbol{W}$	=	flow solution vector
a_∞	=	freestream speed of sound, *m/s*
c	=	blade chord, *m*
c_{ref}	=	reference blade chord, *m*
C_P	=	blade sectional pressure coefficient, $C_P = \dfrac{P - P_\infty}{1/2\rho_\infty(\Omega r)^2}$
C_Q	=	rotor torque coefficient, $C_Q = \dfrac{Q}{\rho_\infty(\Omega R)^2\pi R^3}$
C_T	=	rotor thrust coefficient, $C_T = \dfrac{T}{\rho_\infty(\Omega R)^2\pi R^2}$
C_{mx}	=	pitch moment
C_{my}	=	roll moment
C_{DO}	=	overall profile drag coefficient
k	=	turbulent kinetic energy, m^2/s^2
k_i	=	induced power factor

[a] PhD Student, CFD Laboratory, School of Engineering, Email: a.jimenez-garcia.1@research.gla.ac.uk
[b] Professor, MAIAA, MRAeS, CFD Laboratory, School of Engineering, Email: George.Barakos@glasgow.ac.uk

M_{tip} = blade-tip Mach number, $M_{\text{tip}} = \dfrac{V_{\text{tip}}}{a_\infty}$

N_b = number of blades

P = pressure, *Pa*

P_∞ = freestream pressure, *Pa*

Q = rotor torque, $N \cdot m$

R = rotor radius, *m*

r = radial coordinate along the blade span, *m*

T = rotor thrust, *N*

V_∞ = freestream velocity, *m/s*

V_{tip} = blade-tip speed, $V_{\text{tip}} = \Omega R$, *m/s*

AR = aspect ratio, R/c_{ref}

FoM = figure of merit, FoM $= \dfrac{C_T^{3/2}}{\sqrt{2}C_Q}$

Re = Reynolds number, Re $= V_{\text{tip}} c_{\text{ref}}/\nu_\infty$

∞ = freestream value

ref = reference value

tip = blade-tip value

β = coning angle, *deg*

γ = intermittency factor

κ_1, κ_2 = MUSCL scheme parameters

μ = advance ratio, $\mu = \dfrac{V_\infty}{V_{\text{tip}}}$

ν_∞ = freestream kinematic viscosity, m^2/s

Ω = rotor rotational speed, *rad/s*

Ψ = local azimuth angle, *deg*

ρ = density, kg/m^3

ρ_∞ = freestream density, kg/m^3

σ	=	rotor solidity, $\sigma = \dfrac{N_b c_{\text{ref}}}{\pi R}$
Θ	=	local blade twist angle, *deg*
θ_{75}	=	blade pitch angle at $r/R = 0.75$, *deg*
ALE	=	arbitrary lagrangian eulerian
ATB	=	advanced technology blade
BET	=	blade element theory
BILU	=	block incomplete lower-upper
BVI	=	blade vortex interaction
CFD	=	computational fluid dynamics
DDES	=	delay-detached-eddy simulation
DES	=	detached eddy simulation
HMB	=	helicopter multi-block
IGE	=	in-ground effect
LES	=	large-eddy simulation
MUSCL	=	monotone upstream-centred schemes for conservation laws
OARF	=	outdoor aeronautical research facility
OGE	=	out-of-ground effect
PSP	=	pressure sensitive paint
SST	=	shear-stress transport
URANS	=	unsteady Reynolds averaged Navier-Stokes

I. Introduction

Recently, significant progress has been made in accurately predicting the efficiency of hovering rotors using Computational Fluid Dynamics (CFD) [1]. The hover condition is an important design point due to its high power consumption. Consequently, accurate prediction of the rotor figure of merit (FoM) along with the strength and position of the vortex core is of practical interest to rotorcraft manufacturers.

Over the years, various approaches have been developed for modelling rotors in hover. The simplest models are based on one-dimensional momentum theory and Blade Element Theory (BET) [2], which do not account for non-ideal flow, viscous losses, and swirl flow loss effects. Hence, the vortex wake of the rotor is not accurately represented for this basic model. Alternatively, prescribed and free-wake approaches have a detailed vortex wake due to the representation of the root and tip vortices, but they still need additional data for the blade loads. More recently, high fidelity approaches based on numerical simulation of the Navier-Stokes equations are being gradually employed partly due to the emergence of parallel clusters, reducing the high computational time associated with these approaches, and progress with accuracy and stability of CFD solvers.

During the eighties, a comprehensive experimental study of four model-scale rotors (UH-60A, S-76, High Solidity, and H-34) in hover, was conducted by Balch [3, 4]. Further work by Balch and Lombardi [5, 6] compared advanced tip configurations for the UH-60A and S-76 rotor blade geometries, again in hover. The Balch and Lombardi S-76 rotor blade was of 1/4.71 scale while the Balch S-76 rotor blade was of 1/5 scale. The effect of using different tip configurations (rectangular, swept, tapered, swept-tapered, and swept-tapered with anhedral) on the performance of the rotors was experimentally investigated in-ground effect (IGE) and out-of-ground effect (OGE) conditions.

To assess the accuracy of the present method in predicting the figure of merit at high disc loading, the XV-15 tiltrotor blade was considered, at first. Very little wind tunnel data is available for model and full-scale tiltrotors. At the early stage of the XV-15 program, the NASA 40-by-80-Foot Wind Tunnel was used to measure integrated rotor loads in helicopter [7], aeroplane and transition-corridor modes [8]. However, force and moment measurements did not exclude the contribution from the airframe. The NASA-Ames Outdoor Aeronautical Research Facility (OARF) was also extensively used by Felker *et al.*[9] with the XV-15 rotor and Bartie *et al.*[10] with the XV-15 Advanced Technology Blade (ATB). The hover and forward flight tests began in the late 90s with the work of Light [11] in the 80-ft by 120-ft wind tunnel at NASA Ames, but only few conditions were tested. To fill this gap, Betzina [12] in 2002 undertook an extensive campaign of experiments on the full-scale XV-15 rotor, where the experiments were corrected for hub and tares effects. For all sets of experiments cited, neither surface pressure nor skin friction coefficients were measured. In this regard, Wadcook *et al.*[13] measured skin friction coefficients on a hovering full-scale XV-15 tiltrotor in the 80-ft by 120-ft wind tunnel at NASA Ames. At low thrust, a region of laminar flow was encountered over a significant fraction of the blade chord, while at high disc loading conditions, the laminar to turbulent transition region on the upper blade surface moved towards the blade leading edge with a fully turbulent boundary layer encountered outboard. This set of experiments can be used to validate and improve flow

transition models for tiltrotors.

The structure of this paper is organised as follows. First, we present an aerodynamic study of the XV-15 and PSP rotors, with high-fidelity computational fluid dynamics. The aim is to assess the level of accuracy of the present CFD method in predicting the figure of merit for a hover cases with modest computer resources. This is addressed by comparing with experimental data available in the literature [9, 11, 12, 14–16]. To reduce the computational cost, we solved the hover flow by casting the equations as a steady-state problem in a noninertial reference frame. Regarding the XV-15 rotor, the impact of a spatial discretisation and a fully-turbulent k-ω SST and transitional k-ω SST-γ models on the predicted figure of merit is shown. The ability of those models in predicting the experimental skin friction distribution [13] on the blade surface is also discussed. Hovering simulations for the PSP blade are also shown at two blade-tip Mach numbers. Finally, flowfield visualisation of the UH-60A rotor in forward flight at high speed is shown.

II. HMB Solver

The Helicopter Multi-Block (HMB) [17–20] code is used as the CFD solver for the present work. It solves the Unsteady Reynolds Averaged Navier-Stokes (URANS) equations in integral form using the arbitrary Lagrangian Eulerian (ALE) formulation, first proposed by Hirt *et al.*[21], for time-dependent domains, that may include moving boundaries. The Navier-Stokes equations are discretised using a cell-centred finite volume approach on a multi-block grid. The spatial discretisation of these equations leads to a set of ordinary differential equations in time,

$$\frac{d}{dt}(\boldsymbol{W}V) = -\boldsymbol{R}(\boldsymbol{W}), \tag{1}$$

where $\boldsymbol{W}$ and $\boldsymbol{R}$ are the flow solution and flux residual vectors, respectively, and V is the volume of the cell. To evaluate the convective fluxes, Osher [22] and Roe [23] approximate Riemann solvers are used in HMB, while the viscous terms are discretised using a second order central differencing spatial discretisation. The Monotone Upstream-centred Schemes for Conservation Laws (MUSCL) developed by van Leer [24] is used to provide third order accuracy in space. The HMB solver uses the alternative form of the Albada limiter [25] being activated in regions where a large gradients are encountered, mainly due to shock waves, avoiding the non-physical spurious oscillations. An implicit, dual-time stepping method is employed to performed the temporal integration. The solution is marching in the pseudo-time to achieve fast convergence, using a first-order backward difference. The linearised system of the Navier-Stokes equations is solved using the Generalised Conjugate Gradient method with a Block Incomplete Lower-Upper (BILU) factorisation as a pre-conditioner [26]. Multi-block structured meshes are used for HMB, which allow easy sharing of the calculation load in parallel computing. Structured multi-block hexa meshes are generated using ICEM-Hexa™.

A. High-Order Formulation

This section describes the formulation of the high-order correction terms. This formulation was firstly proposed by Burg [27] for unstructured finite volume codes, where a third-order spatial accuracy was achieved for two-and three-dimensional problems. Yang *et al.*[28, 29] extended the scheme to fourth-order spacial accuracy. The scheme developed, closely resembles the MUSCL-schemes [24]. This scheme is compact, and used here to discretised the convective part of the Navier–Stokes equations. It represents a one-parameter family of equations, where a third-order spatial accuracy can be achieved. For 1-dimensional problems and uniform spacing, the extrapolation to both sides of the face located at $i+1/2$ for a MUSCL-scheme is given:

$$\begin{aligned} \mathbf{F}^{L}_{i+1/2} &= \mathbf{F}_i + \left[\frac{\kappa_1}{2}(\mathbf{F}_{i+1}-\mathbf{F}_i) + (1-\kappa_1)\vec{\nabla}\mathbf{F}_i \bullet \vec{\mathbf{r}}_{f_i}\right] \\ \mathbf{F}^{R}_{i+1/2} &= \mathbf{F}_{i+1} - \left[\frac{\kappa_1}{2}(\mathbf{F}_{i+1}-\mathbf{F}_i) + (1-\kappa_1)\vec{\nabla}\mathbf{F}_{i+1} \bullet \vec{\mathbf{r}}_{f_{i+1}}\right] \end{aligned} \tag{2}$$

which are at least second-order accurate for all values of k_1. By setting $k_1 = 0$, a 2nd-order upwind scheme is obtained. If $k_1 = 1/3$, the method is third-order accurate, which is referred in the literature to as "third-order upwind biased" [30]. However, if k_1 is set to 1, a 2nd-order central difference scheme is obtained.

In the Eq. 2 the vectors $\vec{\mathbf{r}}_{f_i}$ and $\vec{\mathbf{r}}_{f_{i+1}}$ represent the distances between the cell-centre face $i+1/2$ and cell-centre volume i, and the cell-centre volume $i+1$ and cell-centre face $i+1/2$, respectively. To reconstruct the gradients $\vec{\nabla}\mathbf{F}_i$ and $\vec{\nabla}\mathbf{F}_{i+1}$ at the cell-centre volumes i and $i+1$, either Green-Gauss or Least-Squares approaches can be considered. It is clear that the present MUSCL-schemes is limited to third-order accurate.

Following Yang [28], the proposed 4th-order structured MUSCL scheme is written in a similar fashion, where the extrapolation to both sides of the face located at $i+1/2$ is given as:

$$\begin{aligned} \mathbf{F}^{L}_{i+1/2} &= \overbrace{\mathbf{F}_i + \frac{\kappa_1}{2}(\mathbf{F}_{i+1}-\mathbf{F}_i) + (1-\kappa_1)\vec{\nabla}\mathbf{F}_i \bullet \vec{\mathbf{r}}_{f_i}}^{\text{Standard MUSCL for the left state}} \\ &\quad \underbrace{+\frac{1}{2}\left[\frac{\kappa_2}{2}\left(\vec{\nabla}\mathbf{F}_{i+1}\bullet\vec{\mathbf{r}}_{f_i} - \vec{\nabla}\mathbf{F}_i\bullet\vec{\mathbf{r}}_{f_i}\right) + (1-\kappa_2)\vec{\nabla}\left(\vec{\nabla}\mathbf{F}_i\bullet\vec{\mathbf{r}}_{f_i}\right)\bullet\vec{\mathbf{r}}_{f_i}\right]}_{\text{High-order corrections for the left state}} \\ \mathbf{F}^{R}_{i+1/2} &= \overbrace{\mathbf{F}_{i+1} - \frac{\kappa_1}{2}(\mathbf{F}_{i+1}-\mathbf{F}_i) - (1-\kappa_1)\vec{\nabla}\mathbf{F}_{i+1} \bullet \vec{\mathbf{r}}_{f_{i+1}}}^{\text{Standard MUSCL for the right state}} \\ &\quad \underbrace{+\frac{1}{2}\left[\frac{\kappa_2}{2}\left(\vec{\nabla}\mathbf{F}_{i+1}\bullet\vec{\mathbf{r}}_{f_{i+1}} - \vec{\nabla}\mathbf{F}_i\bullet\vec{\mathbf{r}}_{f_{i+1}}\right) + (1-\kappa_2)\vec{\nabla}\left(\vec{\nabla}\mathbf{F}_{i+1}\bullet\vec{\mathbf{r}}_{f_{i+1}}\right)\bullet\vec{\mathbf{r}}_{f_{i+1}}\right]}_{\text{High-order corrections for the right state}} \end{aligned} \tag{3}$$

As can be observed, this new variable extrapolation formulation represents a two-parameter family (k_1 and k_2), and is equivalent to the standard MUSCL-scheme under certain values of k_1 and k_2. As shown in the Eq. 3, the high-order correction terms have been developed using a Taylor series expansion about the centre of the face $i+1/2$, which requires knowledge of its second derivate $\vec{\nabla}\left(\vec{\nabla}\mathbf{F}_i \bullet \vec{\mathbf{r}}_{f_i}\right)$. Once the first derivatives are computed, the second derivatives can be calculated by successive application of the Green-Gauss or Least Square Method to the first derivatives.

$$
\begin{aligned}
\mathbf{F}^{L}_{i+1/2} \;=\; & \mathbf{F}_i + \frac{\kappa_1}{2}(\mathbf{F}_{i+1} - \mathbf{F}_i) + (1-\kappa_1)\vec{\nabla}\mathbf{F}_i \bullet \vec{\mathbf{r}}_{f_i} \\
& + \frac{1}{2}\left[\frac{\kappa_2 \Delta \mathrm{x}_{f_i}}{2}\left((\frac{\partial \mathbf{F}}{\partial \mathrm{x}})_{i+1} - (\frac{\partial \mathbf{F}}{\partial \mathrm{x}})_i\right) + (1-\kappa_2)\Delta \mathrm{x}_{f_i}\vec{\nabla}\left(\frac{\partial \mathbf{F}}{\partial \mathrm{x}}\right)_i \bullet \vec{\mathbf{r}}_{f_i}\right] \\
& + \frac{1}{2}\left[\frac{\kappa_2 \Delta \mathrm{y}_{f_i}}{2}\left((\frac{\partial \mathbf{F}}{\partial \mathrm{y}})_{i+1} - (\frac{\partial \mathbf{F}}{\partial \mathrm{y}})_i\right) + (1-\kappa_2)\Delta \mathrm{y}_{f_i}\vec{\nabla}\left(\frac{\partial \mathbf{F}}{\partial \mathrm{y}}\right)_i \bullet \vec{\mathbf{r}}_{f_i}\right] \\
& + \frac{1}{2}\left[\frac{\kappa_2 \Delta \mathrm{z}_{f_i}}{2}\left((\frac{\partial \mathbf{F}}{\partial \mathrm{z}})_{i+1} - (\frac{\partial \mathbf{F}}{\partial \mathrm{z}})_i\right) + (1-\kappa_2)\Delta \mathrm{z}_{f_i}\vec{\nabla}\left(\frac{\partial \mathbf{F}}{\partial \mathrm{z}}\right)_i \bullet \vec{\mathbf{r}}_{f_i}\right]
\end{aligned}
\tag{4}
$$

$$
\begin{aligned}
\mathbf{F}^{R}_{i+1/2} \;=\; & \mathbf{F}_{i+1} - \frac{\kappa_1}{2}(\mathbf{F}_{i+1} - \mathbf{F}_i) - (1-\kappa_1)\vec{\nabla}\mathbf{F}_{i+1} \bullet \vec{\mathbf{r}}_{f_{i+1}} \\
& + \frac{1}{2}\left[\frac{\kappa_2 \Delta \mathrm{x}_{f_{i+1}}}{2}\left((\frac{\partial \mathbf{F}}{\partial \mathrm{x}})_{i+1} - (\frac{\partial \mathbf{F}}{\partial \mathrm{x}})_i\right) + (1-\kappa_2)\Delta \mathrm{x}_{f_{i+1}}\vec{\nabla}\left(\frac{\partial \mathbf{F}}{\partial \mathrm{x}}\right)_{i+1} \bullet \vec{\mathbf{r}}_{f_{i+1}}\right] \\
& + \frac{1}{2}\left[\frac{\kappa_2 \Delta \mathrm{y}_{f_{i+1}}}{2}\left((\frac{\partial \mathbf{F}}{\partial \mathrm{y}})_{i+1} - (\frac{\partial \mathbf{F}}{\partial \mathrm{y}})_i\right) + (1-\kappa_2)\Delta \mathrm{y}_{f_{i+1}}\vec{\nabla}\left(\frac{\partial \mathbf{F}}{\partial \mathrm{y}}\right)_{i+1} \bullet \vec{\mathbf{r}}_{f_{i+1}}\right] \\
& + \frac{1}{2}\left[\frac{\kappa_2 \Delta \mathrm{z}_{f_{i+1}}}{2}\left((\frac{\partial \mathbf{F}}{\partial \mathrm{z}})_{i+1} - (\frac{\partial \mathbf{F}}{\partial \mathrm{z}})_i\right) + (1-\kappa_2)\Delta \mathrm{z}_{f_{i+1}}\vec{\nabla}\left(\frac{\partial \mathbf{F}}{\partial \mathrm{z}}\right)_{i+1} \bullet \vec{\mathbf{r}}_{f_{i+1}}\right]
\end{aligned}
\tag{5}
$$

The present high-order formulation requires optimal values of k_1 and k_2 to assure higher-order of accuracy. In this regard, we derive the order of accuracy of the scheme in 1D, considering the approximation of the derivate at the nodes as:

$$
\begin{aligned}
& \int_{x-\frac{1}{2}}^{x+\frac{1}{2}} \frac{\partial \mathbf{F}}{\partial x} dx \approx \mathbf{F}^{L}_{i+\frac{1}{2}} - \mathbf{F}^{L}_{i-\frac{1}{2}} \\
& = \frac{1+\kappa_2}{32}\mathbf{F_{i+2}} + \frac{7+8\kappa_1-3\kappa_2}{32}\mathbf{F_{i+1}} + \frac{11-12\kappa_1+\kappa_2}{16}\mathbf{F_i} \\
& + \frac{-19+12\kappa_1+\kappa_2}{16}\mathbf{F_{i-1}} + \frac{9-8\kappa_1-3\kappa_2}{32}\mathbf{F_{i-2}} + \frac{-1+\kappa_2}{32}\mathbf{F_{i-3}} \\
& = \mathbf{F}'_i \Delta x + \frac{1+6\kappa_1}{24}\mathbf{F}'''_i \Delta x^3 + \frac{1-2\kappa_1+\kappa_2}{16}\mathbf{F}^{(4)}_i \Delta x^4 + O(\Delta x^5)
\end{aligned}
\tag{6}
$$

One can observe that this formula is at least 2nd-order accurate for all values of κ_1 and κ_2, while if $\kappa_1 = -\frac{1}{6}$ and $\kappa_2 = -\frac{4}{3}$, the approximation of the derivate at the node is 4th-order accurate, with no mechanism of dissipation. Moreover, a low dissipation δ can be introduced to reduce spurious oscillation and at the same time maintain the high-order accuracy when κ_2 is set to $-\frac{4}{3} + \delta$.

B. Turbulence and Transition Models

Various turbulence models are available in HMB, including several one-equation, two-equation, three-equation, and four-equation turbulence models. Furthermore, Large-Eddy Simulation (LES), Detached-Eddy Simulation (DES), and Delay-Detached-Eddy Simulation (DDES) are also available. For this study, two and three equations models were employed using the fully-turbulent k-ω SST and the transitional model k-ω SST-γ both from Menter [31, 32]. It is well known that the fully-turbulent k-ω SST model predicts the transition onset further upstream than what is measured in tests, requiring the use of transition models. In this regard, Menter *et al.*[33] developed a model for the prediction of laminar-turbulent transitional flows, involving two transport equations for the intermittency factor γ and the momentum thickness Reynolds number Re_θ. The intermittency factor γ is used to trigger and control the transition onset location, and it varies between 0 (laminar flow) to 1 (fully-turbulent flow). In 2015, a new one-equation local correlation-based transition model γ was proposed by Menter *et al.*[32], where the Re_θ equation was avoided. The form of the transport equation for the intermittency factor γ reads as:

$$\frac{\partial(\rho\gamma)}{\partial t} + \frac{\partial(\rho U_j\gamma)}{\partial x_j} = P_\gamma - E_\gamma + \frac{\partial}{\partial x_j}\left[\left(\mu + \frac{\mu_t}{\sigma_\gamma}\right)\frac{\partial\gamma}{\partial x_j}\right] \tag{7}$$

where P_γ and E_γ represent the production and destruction sources respectively. A more detailed description of the γ equation can be found in [32].

III. XV-15 Tiltrotor Blade

A. XV-15 Rotor Geometry

The three-bladed XV-15 rotor geometry was generated based on the full-scale wind tunnel model tested by Betzina in the NASA Ames 80- by 120-foot wind tunnel facility [12]. NACA 6-series five-digit aerofoil sections comprise the rotor blade as reported in Table 1.

Table 1: Radial location of the XV-15 rotor blade aerofoils [9].

$\mathbf{r/R}$	**Aerofoil**
0.09	NACA 64-935
0.17	NACA 64-528
0.51	NACA 64-118
0.80	NACA 64-(1.5)12
1.00	NACA 64-208

The main geometric characteristics of the XV-15 rotor blades [12] are summarised in Table 2. It is interesting to note that unlike convectional helicopter blades, tiltrotor blades are characterised by high twist and solidity, along with a small rotor radius.

A detailed sketch of the XV-15 blade planform and the blade radial twist, and chord distributions are shown in Figure 1. The rotor blade chord is held constant, and extends at almost 80% of the rotor blade. The blade root, however, was not modelled due to the lack of information on the cuff geometry in the literature.

Table 2: Geometric properties of the full-scale XV-15 rotor [12].

Parameter	**Value**
Number of blades, N_b	3
Rotor radius, R	150 inches
Reference blade chord, c_{ref}	14 inches
Aspect ratio, R/c_{ref}	10.71
Rotor solidity, σ	0.089
Linear twist angle, Θ	-40.25°

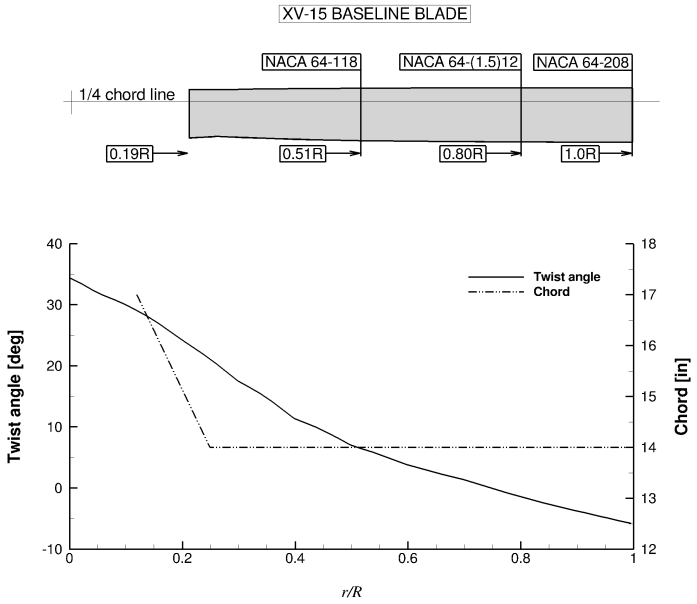

Fig. 1: Planform of the XV-15 rotor blade (above) and twist and chord distributions [34] (below).

B. XV-15 Rotor Mesh

A mesh generated using the chimera technique was used for the aerodynamic study of the XV-15 rotor. It includes a cylindrical off-body mesh used as background, and a body-fitted mesh for the blade. The use of an overset grid method allowed for the blade pitch angle to be changed by rotating the body-fitted mesh. Because the XV-15 rotor was numerically evaluated in hover and propeller modes (axial flight), only a third of the computational domain was meshed, assuming periodic conditions for the flowfield in the azimuthal direction (not applicable to stall condition). A view of the computational domain, along with the boundary conditions employed is given in Figure 2 (a). Farfield boundaries were extended to $2R$ (above rotor) and $4R$ (below rotor and in the radial direction) from the rotor plane, which assures an independent solution with the boundary conditions employed. Furthermore, an ideal rotor hub was modelled and approximated as a cylinder, extending from inflow to outflow with a radius of $0.05R$.

A C-topology was selected for the leading edge of the blade, while an H-topology was employed at the trailing edge. This configuration permits an optimal resolution of the boundary layer due to the orthogonality of the cells around the surface blade (Figure 2 (b)). The height of the first mesh layer above the blade surface was set to $1.0 \cdot 10^{-5} c_{\text{ref}}$, which leads to y^+ less than 1.0 all over the blade. Considering the chordwise and spanwise directions of the blade, 264 and 132 mesh points were used, while the blunt trailing-edge was modelled with 42 mesh points.

To guarantee a mesh independent solution, two computational domains were built. Table 3 lists the grids used and shows the breakdown of cells per blade. The coarse and medium meshes have 6.2 and 9.6 million cells per blade (equivalent to 18.6 and 28.8 million cells for three blades), with the same grid resolution

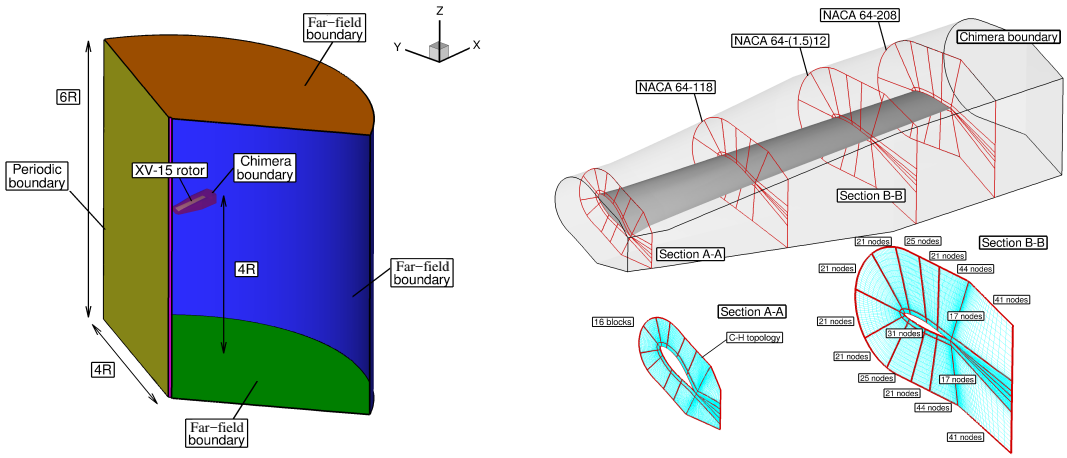

(a) Computational domain.

(b) XV-15 rotor mesh.

Fig. 2: Computational domain and boundary conditions employed (left) and detailed view of the XV-15 rotor mesh (right).

for the body-fitted mesh (3.6 million cells). The background mesh, however, was refined at the wake and near-body regions, increasing the grid size from 2.6 to 6 million cells.

Table 3: Meshing parameters for the XV-15 rotor mesh.

	Coarse Mesh	**Medium Mesh**
Background mesh size (cells)	2.6 million	6.0 million
Blade mesh size (cells)	3.6 million	3.6 million
Overall mesh size (cells)	6.2 million	9.6 million
Height of the first mesh layer at blade surface	$1.0 \cdot 10^{-5} c_{\text{ref}}$	$1.0 \cdot 10^{-5} c_{\text{ref}}$

C. Effect of the Spatial Discretisation

This section demonstrates the performance of the MUSCL-4 scheme with the chimera technique for the flow around the three-bladed XV-15 rotor [12], solved in hover by casting the equations as a steady-state problem in a noninertial reference frame. The MUSCL-4 scheme is compared with the compact scheme MUSCL-2 in terms of integrated airloads (FoM, C_T, and C_Q), visualisation of the wake flow features, and wake structure (radial and vertical displacements of the vortex). All flow solutions were computed using RANS, coupled with Menter's k-ω SST turbulence model [31]. The flow equations were integrated with the implicit dual-time stepping method of HMB.

Figure 3 shows the effect of the MUSCL-2 and MUSCL-4 schemes on the figure of merit and torque coefficient for the full-scale XV-15 rotor. Experimental data is also shown, carried out by Felker *et al.*[9] at OARF, and Light [11] and Betzina [12] at the NASA 80×120ft wind tunnel. Vertical lines labelled as empty (4,574 kg) and maximum gross (6,000 kg) weight, define the hovering range of the XV-15 helicopter

rotor [35]. Momentum-based estimates of the figure of merit [36] are also included, where an induced power factor k_i of 1.1 and overall profile drag coefficient C_{DO} of 0.01 were used. Polynomial fit curves were computed using the obtained CFD results and shown with solid lines and squares (MUSCL-2 with a coarse grid), deltas (MUSCL-2 with a medium grid), and triangles (MUSCL-4 with a coarse grid). The CFD results obtained with the MUSCL-2 scheme present a good agreement with the test data of Betzina [12] for all blade collective angles. Moreover, the effect of the grid size has a mild effect on the overall performance at low thrust, with a small influence at high thrust. Regarding the results obtained with the MUSCL-4 scheme, a good agreement was obtained if compared with the MUSCL-2 scheme when using a medium grid, and the experimental data of Betzina.

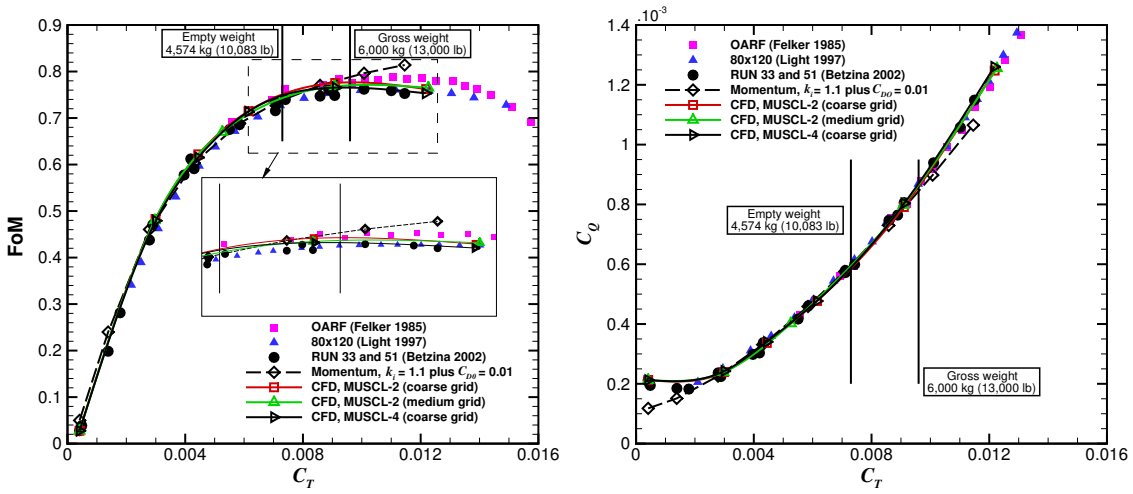

(a) FoM - C_T.

(b) C_Q - C_T.

Fig. 3: Effect of the MUSCL-2 and MUSCL-4 schemes on the figure of merit (left) and torque coefficient (right) for the full-scale XV-15 rotor.

To assess the ability of the MUSCL-4 scheme in accurately predicting the loads when a coarse mesh is employed, a comparison between predicted and measured [13, 37] FoM at a collective pitch angle of 10° is reported in Table 4. Predictions with the MUSCL-2 scheme using coarse and medium grids indicate good correlation with the experiments (1.5 and 0.8 counts of FoM, respectively). Results obtained with the MUSCL-4 scheme on a coarse grid present a small discrepancy of 0.5 counts of FoM with respect to experiments, which highlights the benefit of using higher-order numerical scheme in accurately predicting integrated airloads.

Despite that the lower-order numerical scheme is sufficient to predict the loads over the blades [38], it did not preserve the near-blade and wake flow features. Those features play a key role in the prediction of the acoustic noise, BVI interactions, and in-ground effects. In hover, to ensure realistic predictions of the wake-induced effects, and therefore induced-drag, the radial and vertical displacements of the vortex core should be resolved, at least for the first and second wake passages.

Table 4: Predicted and experimental [13, 37] figure of merit at collective pitch angle of 10°.

Case	FoM	Difference [%]
Experiment	0.760	-
MUSCL-2 coarse grid	0.775	1.97%
MUSCL-2 medium grid	0.768	1.05%
MUSCL-4 coarse grid	0.765	0.65%

Figure 4 shows the wake flow-field for the full-scale XV-15 rotor using iso-surfaces of Q-criterion obtained with MUSCL-2 (a) and MUSCL-4 (b) with the same coarse grid of Table 3. It should be mentioned that, a collective pitch angle of 10° degrees was selected for such comparison. It is observed that the MUSCL-4 scheme preserves much better the helical vortex filaments that trail from each of the tip-blade, and the wake sheets trailed along the trailing edge of the blade if compared with the MUSCL-2 solution. Therefore, the lower dissipation of the MUSCL-4 scheme results in an improved preservation of rotor wake structures. In this regard, if the MUSCL-2 is employed, the vorticity of the vortex cores (computed using the local vorticity maxima criterion) is significantly dissipated at a wake age of $2\pi/3$ (first blade passage in Figure 5) if compared with MUSCL-4 results. Likewise, at wake ages of $4\pi/3$ (second blade passage) and 2π (third blade passage) a reduction of vorticity by 42.8% and 45.2% is observed when MUSCL-2 is employed.

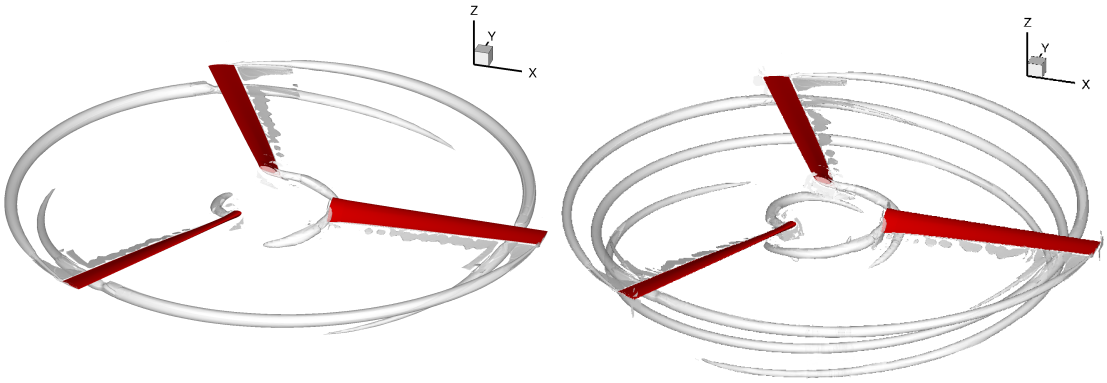

(a) Wake flow using MUSCL-2 scheme.

(b) Wake flow using MUSCL-4 scheme.

Fig. 4: Wake flow-field for the full-scale XV-15 rotor using iso-surfaces of Q-criterion obtained with MUSCL-2 (left) and MUSCL-4 (right) schemes.

Figure 6 shows a comparison of the radial (a) and vertical (b) displacements of the tip vortices, as functions of the wake age (in degrees), with the prescribed wake-models of Kocurek and Tangler [39] and Landgrebe [40]. Like the previous plots, the MUSCL-2 and MUSCL-4 schemes with the coarse grid at blade pitch angle of 10° degrees were selected for comparison. It is seen that the radial displacement is less

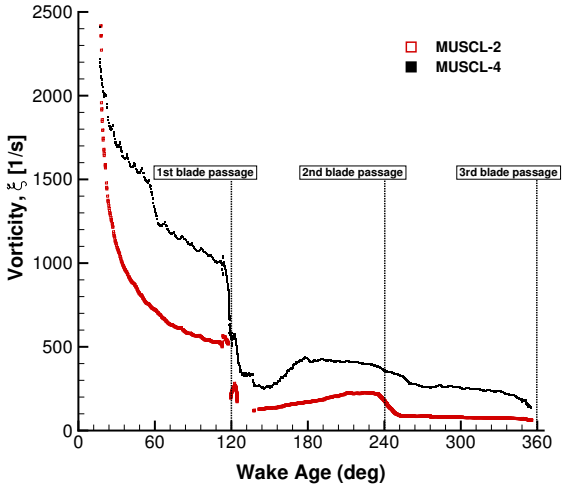

Fig. 5: Vorticity of the vortex cores as function of the wake age in degrees obtained with the MUSCL-2 and MUSCL-4 schemes on the coarse grid.

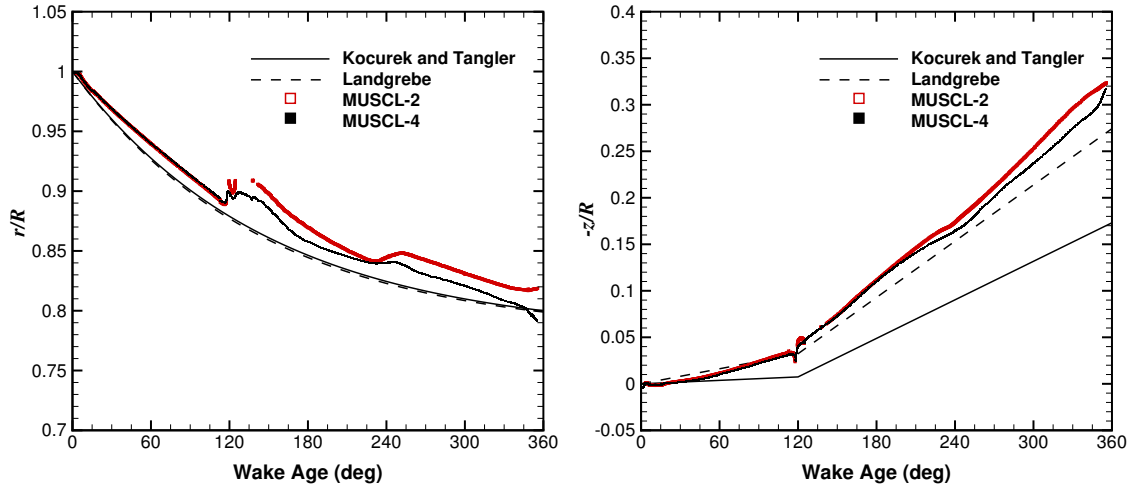

(a) Radial displacements of the tip vortices.

(b) Vertical displacements of the tip vortices.

Fig. 6: Comparison between the radial (above) and vertical (below) tip vortex displacements computed with the MUSCL-2 and MUSCL-4 schemes.

sensitive to changes on the prescribed wake-models that the vertical displacement. Until the first passage (wake age of 120°), a slow convection of the tip vortices is seen in vertical displacement ($-z/R$) and compares very well with Landgrebe model. The MUSCL-2 scheme showed a higher dissipation rate.

D. Effect of the Turbulence Model

In this study, the effect of the $k-\omega$ SST-γ transition model is investigated in predicting the figure of merit. The predicted skin friction coefficient is compared with measurements by Wadcock *et al.*[13]. Moreover, a comparison with the solution obtained with the fully-turbulent k-ω SST model is presented. For this case, a matched grid was used, which has 10.2 million cells per blade.

Figures 7 and 8 show the computed skin friction coefficient C_f compared with the available experimental data of Wadcock for collective pitch angles of 3° and 10° at the radial stations $r/R = 0.28, 0.50, 0.72, 0.83$ and 0.94. At low disc loading (Figure 7), the experiment shows a natural transition for all stations at about 50% chord. It seems that the present transition model is able to capture the onset and length of the natural transition with some discrepancies found at the inboard station $r/R = 0.28$. As expected, results obtained with the fully-turbulent model indicate lack of transition. Moreover, the values of skin friction coefficient are under and over-predicted in the laminar and turbulent flow regions. Considering the C_f at collective pitch angle of 10° (Figure 8), the experimental C_f presents a similar pattern as seen for the lower collective pitch angles. However, the onset of the natural transition is moved towards the leading edge, with a fully-turbulent flow region observed at the outboard station $r/R = 0.94$. Results corresponding to the transition model accurately predicted the onset location and length of the transition. This physical phenomenon is not captured by the fully-turbulent solution. The surface skin friction coefficient of both turbulence models is shown in Figure 9, where the laminar-turbulent region can be only identified for the k-ω SST-γ model.

Once the distribution of skin friction coefficient was analysed, the impact of the turbulence model on the hover performance of the XV-15 blade was investigated. Table 5 reports the predicted C_T, C_Q, and FoM using the fully-turbulent $k-\omega$ SST and transition model k-ω SST-γ at two disc loading conditions. It is shown that results are mildly sensitive to the turbulence model employed, with a higher figure of merit presented by the transition model.

	$\mathbf{C_T}$	$\mathbf{C_Q}$	**FoM**
FT 3°	0.00293	0.000249	0.450
TM 3°	0.00297	0.000223	0.512
FT 10°	0.00906	0.000807	0.756
TM 10°	0.00909	0.000803	0.763

Table 5: Comparison of predicted C_T, C_Q, and FoM at 3° and 10° collective angles between the fully-turbulent $k-\omega$ SST and transition model k-ω SST-γ. Conditions employed: $M_{\text{tip}} = 0.69$ and $Re = 4.95 \cdot 10^6$. FT=Fully-Turbulent; TM=Transitional-Model.

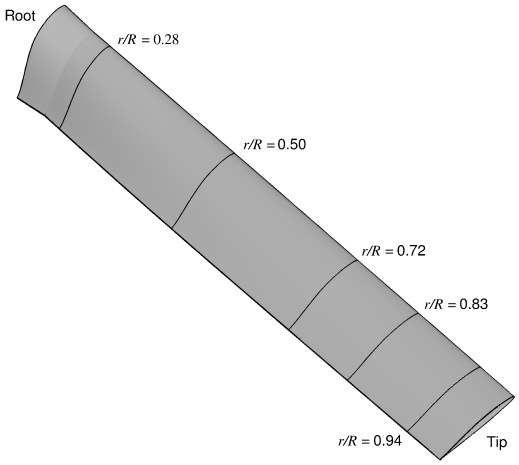

(a) Radial stations.

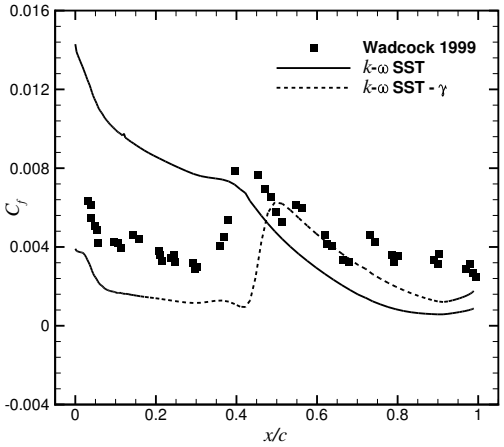

(b) $r/R = 0.28$.

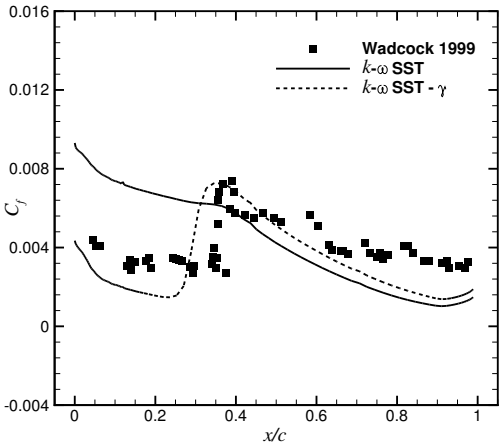

(c) $r/R = 0.50$.

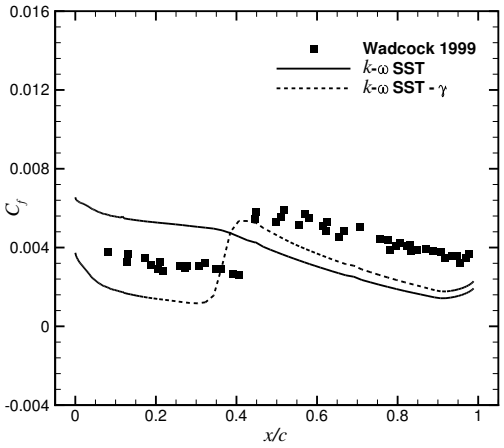

(d) $r/R = 0.72$.

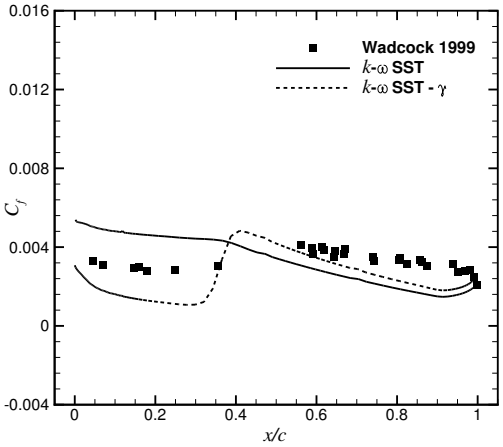

(e) $r/R = 0.83$.

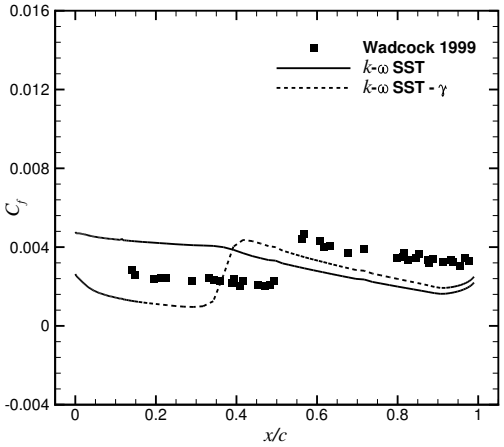

(f) $r/R = 0.94$.

Fig. 7: Comparison between the computed skin friction coefficient using a fully turbulent and transition model solutions with the experimental data of Wadcock *et al.*[13]. Conditions employed: $M_{\text{tip}} = 0.69$, $Re = 4.95 \cdot 10^6$, and $\theta_{75} = 3°$.

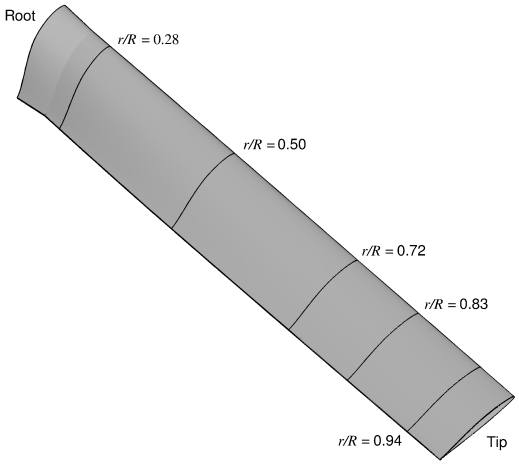

(a) Radial stations.

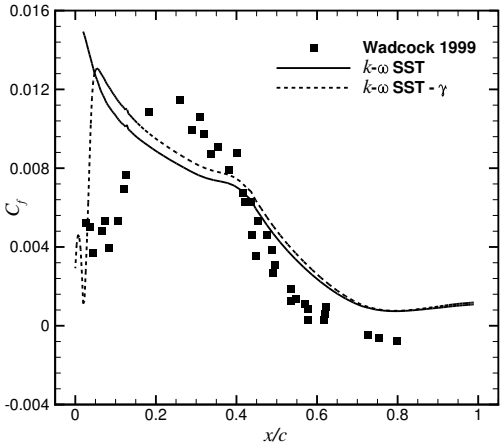

(b) $r/R = 0.28$.

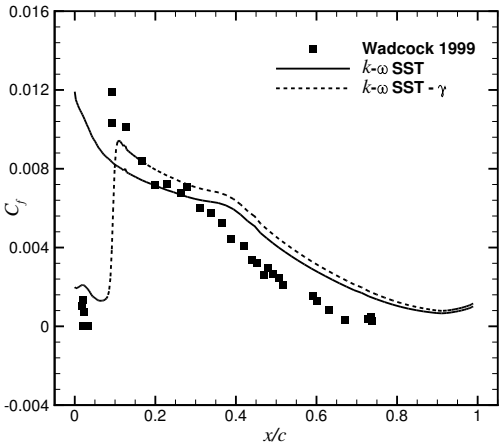

(c) $r/R = 0.50$.

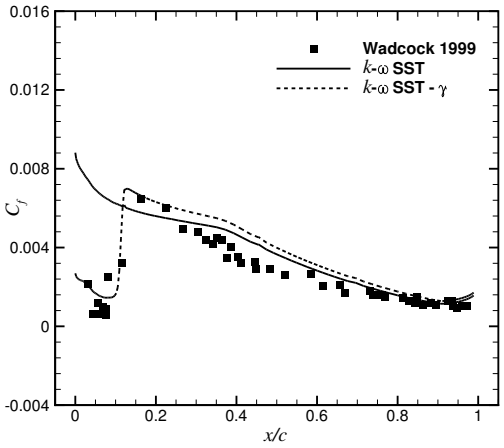

(d) $r/R = 0.72$.

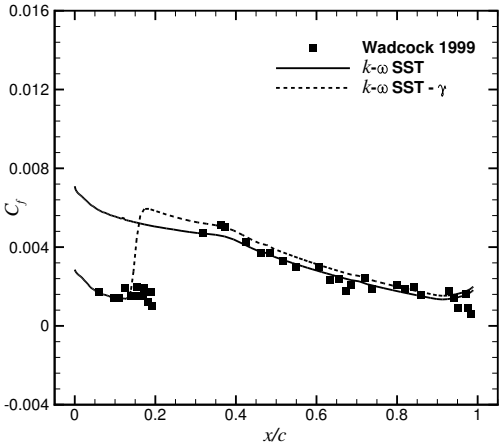

(e) $r/R = 0.83$.

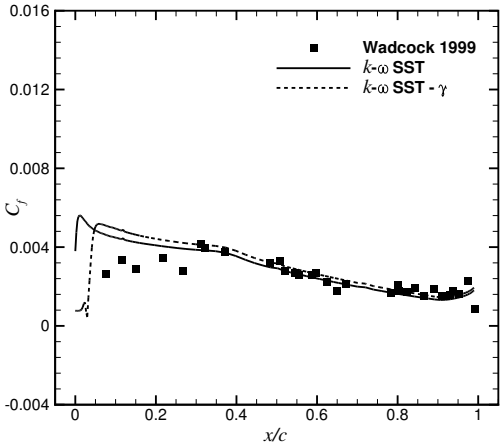

(f) $r/R = 0.94$.

Fig. 8: Comparison between the computed skin friction coefficient using a fully turbulent and transition model solutions with the experimental data of Wadcock *et al.*[13]. Conditions employed: $M_{\text{tip}} = 0.69$, $Re = 4.95 \cdot 10^6$, and $\theta_{75} = 10°$.

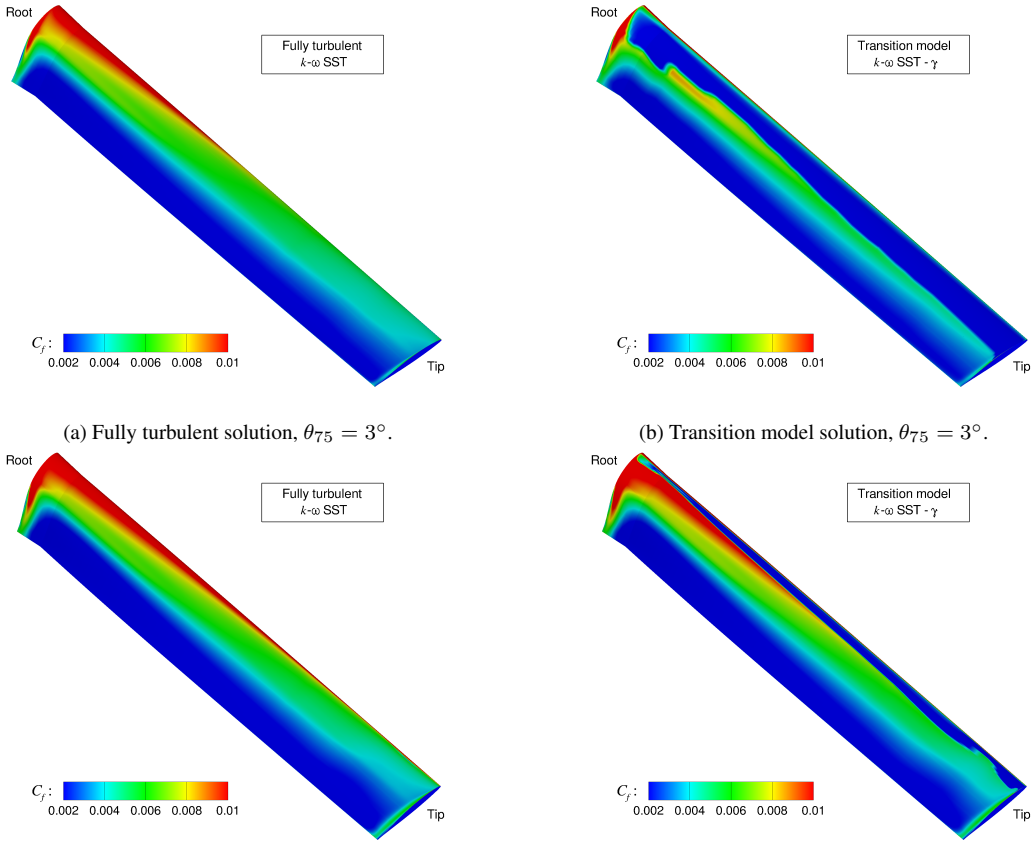

(a) Fully turbulent solution, $\theta_{75} = 3°$.

(b) Transition model solution, $\theta_{75} = 3°$.

(c) Fully turbulent solution, $\theta_{75} = 10°$.

(d) Transition model solution, $\theta_{75} = 10°$.

Fig. 9: Surface skin friction coefficient for the fully turbulent and transition model cases.

IV. PSP Helicopter Blade

A study of the performance of the PSP (Pressure Sensitive Paint) rotor in hover was also carried out. The radius of the PSP rotor is $R = 66.5$ inches, and the reference chord of the blade is $c_{\text{ref}} = 5.45$ inches. Unlike the XV-15 rectangular planform, the PSP's planform includes a 60% taper and 30° swept-back tip. The main geometric characteristics of the PSP rotor blades [15] are summarised in Table 6.

Table 6: Geometric properties of the PSP rotor [14].

Parameter	Value
Number of blades, N_b	4
Rotor radius, R	66.5 inches
Reference blade chord, c_{ref}	5.45 inches
Aspect ratio, R/c_{ref}	12.20
Rotor solidity, σ	0.1033
Linear twist angle, Θ	-14°

Table 7 summarises the conditions employed and computations performed in hover configurations. Two

blade-tip Mach numbers were set, 0.585 and 0.65. The Reynolds number, based on the reference blade chord of 5.45 inches and on the tip speed, was $1.92 \cdot 10^6$ and $2.16 \cdot 10^6$, respectively. All flow solutions were computed by solving the RANS equations, coupled with Menter's k-ω SST turbulence model [31].

Table 7: Flow conditions for the PSP blade.

Thrust coefficient C_T	**Collective θ_{75}**	**Blade-tip Mach number M_{tip}**
0.00259	4.0	0.585
0.00503	6.58	0.585
0.00694	8.48	0.585
0.00797	9.46	0.585
0.00893	10.3	0.585
0.00451	6.0	0.65
0.00552	7.0	0.65
0.00657	8.0	0.65
0.00767	9.0	0.65
0.00881	10.0	0.65
0.00985	11.0	0.65
0.01070	12.0	0.65

Figure 10 shows predictions against published data by Vieira *et al.*[41] using the STAR-CCM+ CFD solver, and experimental data of Overmeyer *et al.*[16]. The HMB results are in excellent agreement with the data. Wong *et al.*[14, 15] also used the PSP technique to measure the sectional blade distribution of C_P at two outboard stations, $r/R = 0.93$ and $r/R = 0.99$. Results in Figures 11-12 suggest that CFD is very accurate for this case.

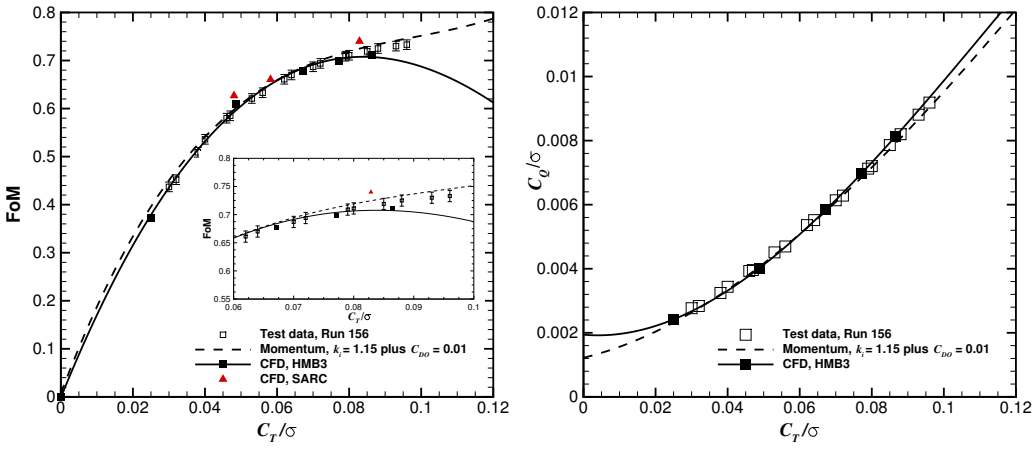

(a) C_T-FoM. (b) C_T/σ-C_Q/σ.

Fig. 10: Integrated blade loads for the PSP model rotor at blade-tip Mach number of 0.585. Comparisons with published numerical [41] and experimental data [16] are also shown. (a) C_T/σ-FoM. (b) C_T/σ-C_Q/σ.

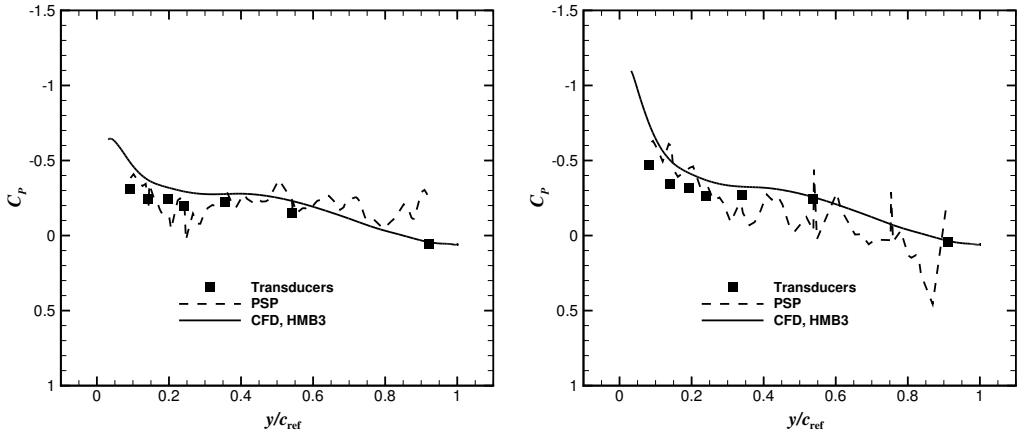

(a) $r/R = 0.93, C_T = 0.005$.

(b) $r/R = 0.93, C_T = 0.007$.

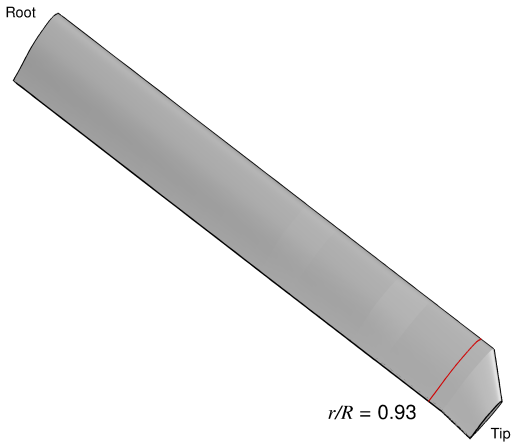

(c) Radial station.

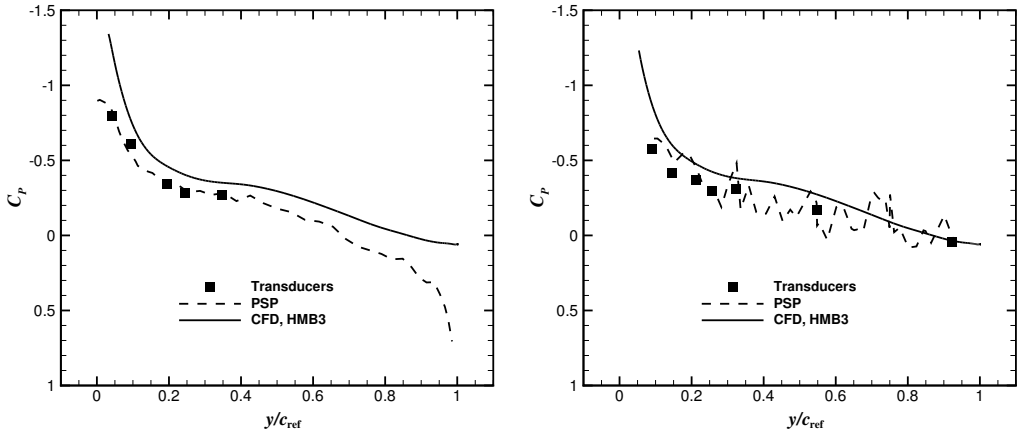

(d) $r/R = 0.93, C_T = 0.008$.

(e) $r/R = 0.93, C_T = 0.009$.

Fig. 11: Comparison between PSP/Pressure tap [14, 15] and CFD at radial station $r/R = 0.93$. (a) $C_T = 0.005$. (b) $C_T = 0.007$. (c) $C_T = 0.008$. (d) $C_T = 0.009$.

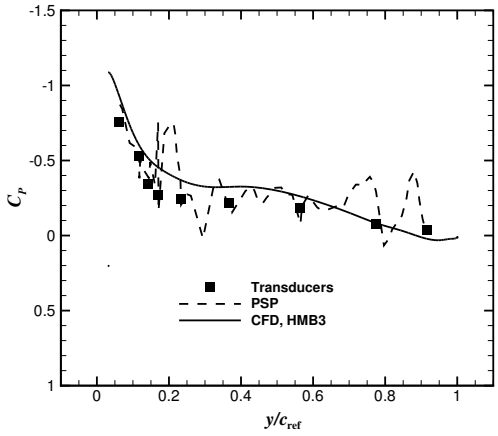

(a) $r/R = 0.99, C_T = 0.005$.

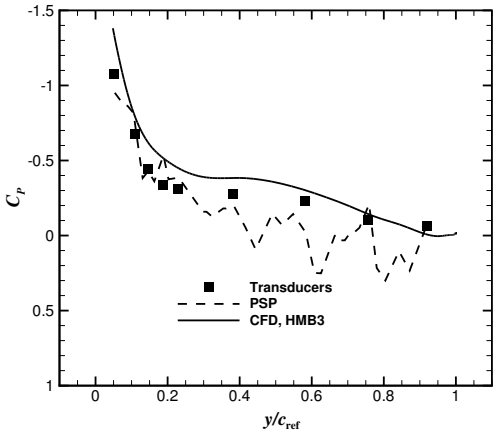

(b) $r/R = 0.99, C_T = 0.007$.

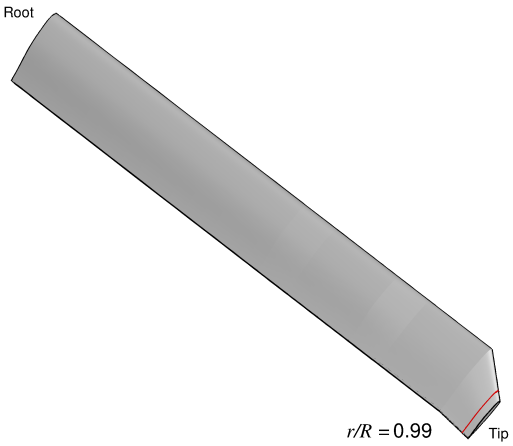

(c) Radial station.

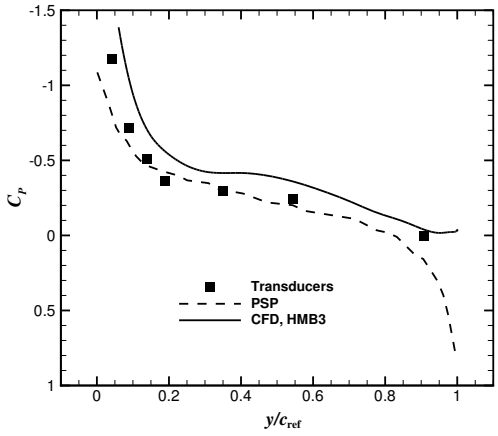

(d) $r/R = 0.99, C_T = 0.008$.

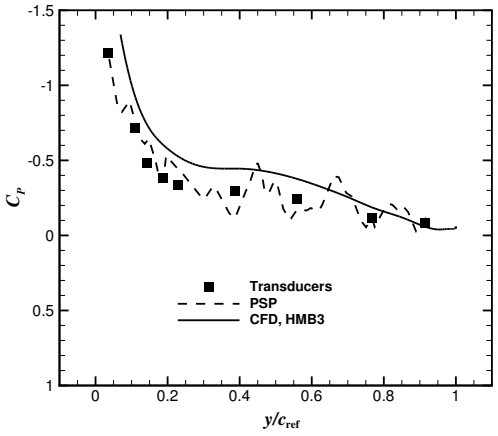

(e) $r/R = 0.99, C_T = 0.009$.

Fig. 12: Comparison between PSP/Pressure tap [14, 15] and CFD at radial station $r/R = 0.99$. (a) $C_T = 0.005$. (b) $C_T = 0.007$. (c) $C_T = 0.008$. (d) $C_T = 0.009$.

Considering the PSP rotor at blade-tip Mach number of 0.65, an overview of the surface pressure coefficient at a collective pitch angle of 11^o is shown in Figure 13a. The vortical structure of the flowfield for the PSP blade is visualised by iso-surface contours of Q-criterion in Figure 13b. This plot reveals that the computations are able to capture the rotor wake up to 3-4 blade passages.

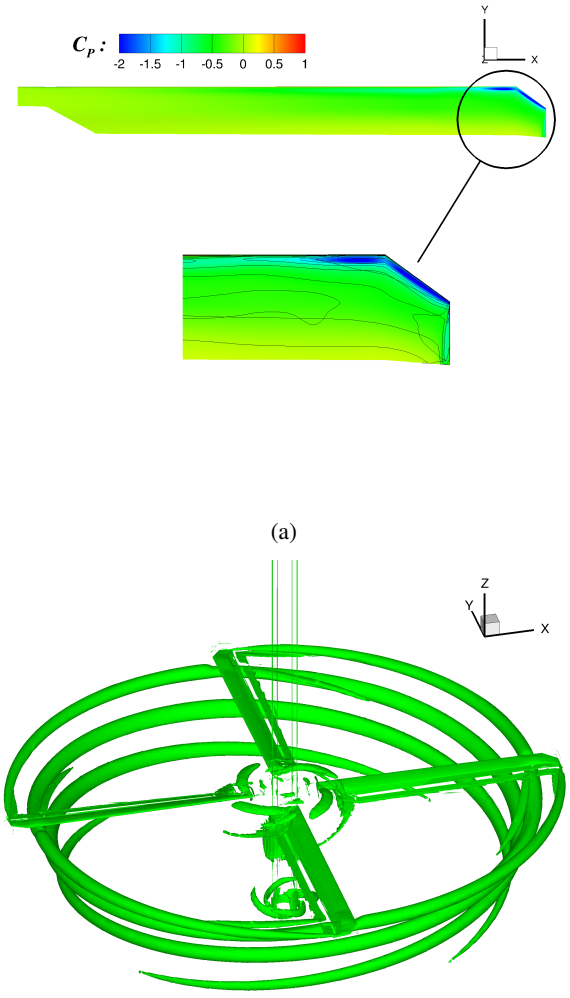

(a)

(b)

Fig. 13: Surface pressure coefficient (above) and wake of the PSP rotor blade (below).

Comparisons for the integrated blade loads are given in Figure 14. Due to the lack of test data, comparisons are shown against published numerical data [42]. Figure 15 shows comparisons with the S-76 tests and predictions, showing the higher performance of the PSP rotor.

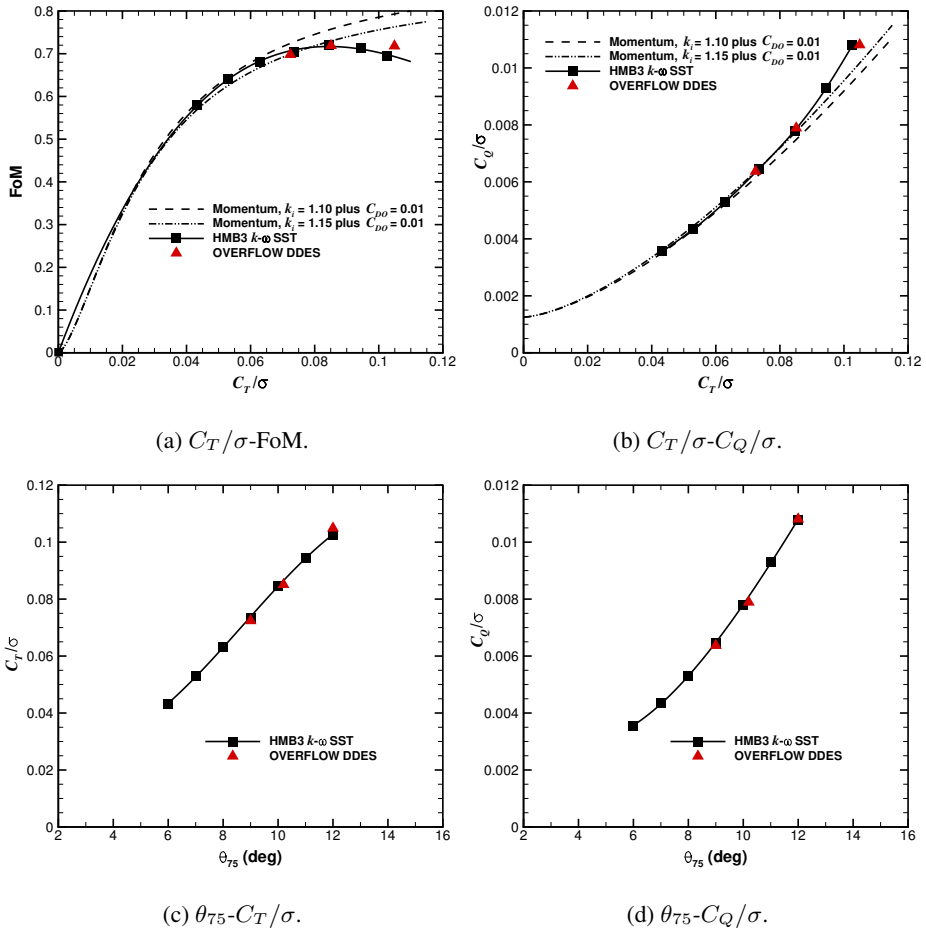

(a) C_T/σ-FoM.

(b) C_T/σ-C_Q/σ.

(c) θ_{75}-C_T/σ.

(d) θ_{75}-C_Q/σ.

Fig. 14: Integrated blade loads for the PSP model rotor at blade-tip Mach number of 0.65. Comparison with published numerical data [42] is also shown. (a) C_T/σ-FoM. (b) C_T/σ-C_Q/σ. (c) θ_{75}-C_T/σ. (d) θ_{75}-C_Q/σ.

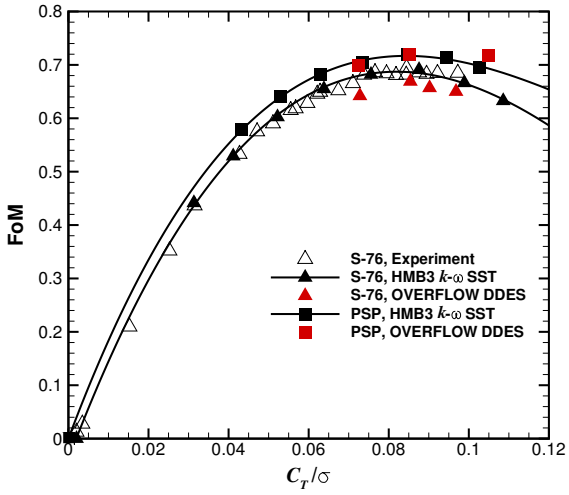

Fig. 15: FoM as function of the thrust coefficient for the 1/4.71 model-scale S-76 rotor with 60% taper and 35° swept tip and PSP rotor computed with HMB and OVERFLOW CFD solvers [42].

V. UH-60A Rotor in Forward Flight

To validate the present high-order scheme for a three-dimensional unsteady flow overset and moving grids, the UH-60A rotor in forward flight was also considered. The UH-60A is a four-bladed rotor made of two aerofoil profiles; the SC-1095 and SC-1095R [43]. The planform of the UH-60A rotor features a 20° swept tip which covers 6% of the blade's radius, with a -16° of linear twist. The main geometric characteristics of the UH-60A blade [5, 44, 45] are summarised in Table 8.

Table 8: Geometric properties of the UH-60A rotor [5, 44, 45].

Parameter	Value
Number of blades, N_b	4
Rotor radius, R	321.96 inches
Reference blade chord, c_{ref}	20.76 inches
Aspect ratio, R/c_{ref}	15.5
Rotor solidity, σ	0.0821
Linear twist angle, Θ	-16°

The multi-block structured grids for the full rotor has a total of 25 million cells with 1848 blocks, with 16.8 and 8.2 million cells for the background and body-fitted grids, respectively. A hub was also included in the computational domain and modelled as a generic ellipsoidal surface.

The test case selected herein for validation corresponds to the UH-60A main rotor at high-speed forward flight. Flight test data corresponding to this demanding configuration (flight C8534) was acquired by the U.S. Army/NASA UH-60A Airloads Program [46]. The rotor advance ratio was μ= 0.368, and the freestream Mach number was set to 0.236. To meet the target thrust coefficient C_T/σ= 0.08 while having zero roll and pitch moments, a matrix trimming method is used in HMB, which uses the blade-element momentum theory to compute the elements of the sensitivity matrix. The trim state is specified in Table 9 and the history of the rotor loads in show in Figure 16.

The flow solutions corresponding to MUSCL-2 and MUSCL-4 schemes were computed by solving the URANS equations, coupled with Menter's k-ω SST turbulence model [31]. The time step corresponds to 0.25 deg in the azimuthal direction and was based on the experience gained with previous rotor computations in forward flight [19].

Figures 17 and 18 show vorticity contours at the planes x/R= 0.5 and 1, respectively, of the blade 1 (ψ= 0) for the MUSCL-2 and MUSCL-4 schemes. Results with MUSCL-4 show a higher resolution of the rotor wake structures at the advancing and retreating sides if compared with the MUSCL-2. In fact, the vortex A ($\psi = 270^\circ$) computed with MUSCL-2 in Figures 17 and 18 shows a reduction of the core vorticity by almost 20% respect to the MUSCL-4 results.

Table 9: Trim state for the UH-60A forward flight case using MUSCL-2 and MUSCL-4 schemes.

Parameter	**Value**	
	MUSCL-2	MUSCL-4
μ	0.368	0.368
M_{tip}	0.648	0.648
θ_{shaft}	7.30°	7.30°
θ_0	12.13°	11.97°
θ_{1s}	8.58°	8.35°
θ_{1c}	-2.27°	-2.17°
β_0	3.43°	3.43°
β_{1s}	-1.0°	-1.0°
β_{1c}	-0.70°	-0.70°

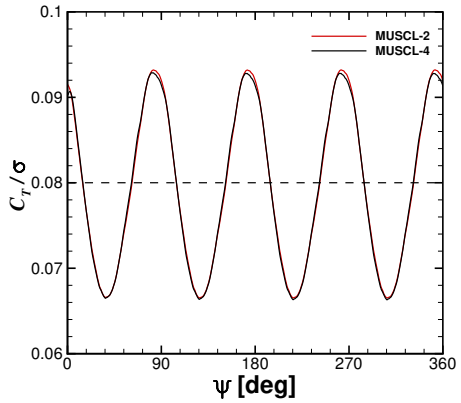

(a) Target thrust coefficient, C_T/σ= 0.08.

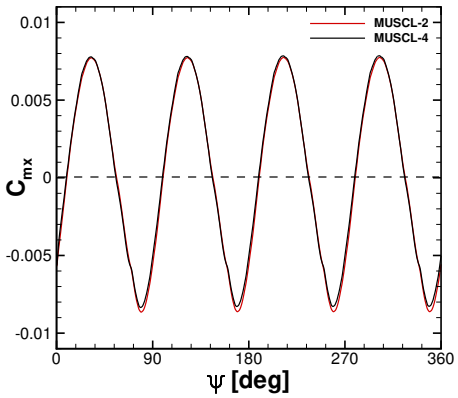

(b) Pitch moment, C_{mx}= 0.

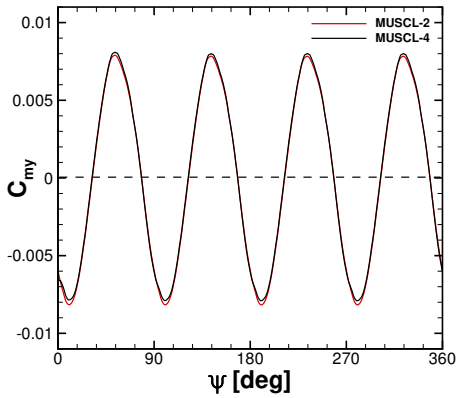

(c) Roll moment, C_{my}= 0.

Fig. 16: Target thrust and zero pitch and roll moment coefficients for the UH-60 rotor in forward flight.

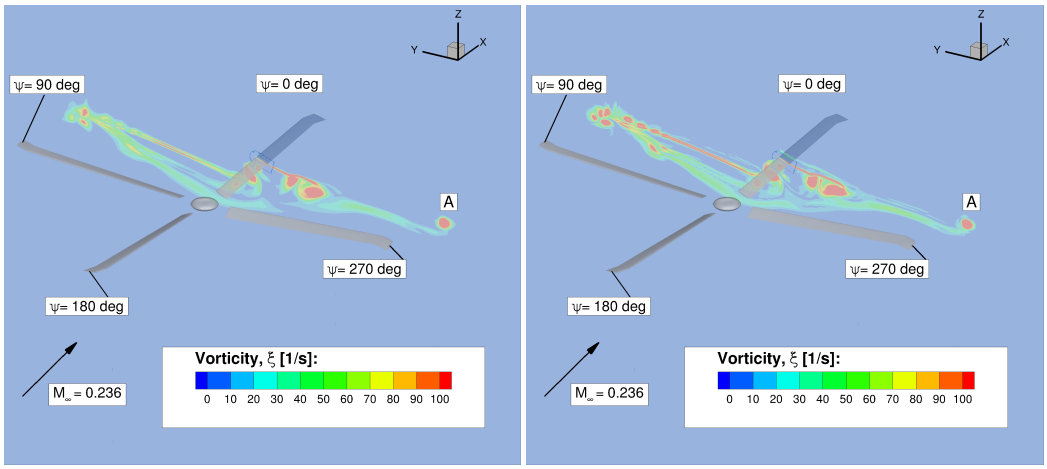

(a) MUSCL-2 scheme. (b) MUSCL-4 scheme.

Fig. 17: Vorticity contours at the plane x/R= 0.5 of the blade 1 (ψ= 0) for the MUSCL-2 and MUSCL-4 schemes.

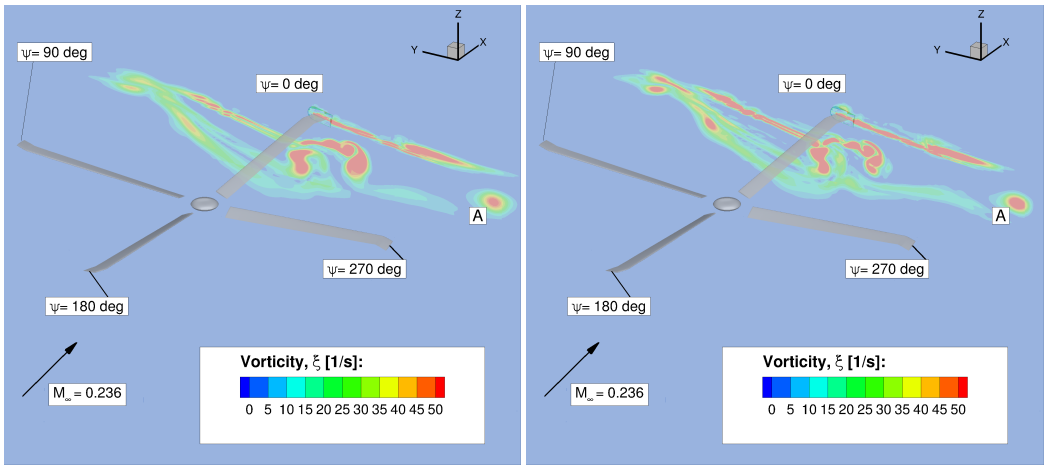

(a) MUSCL-2 scheme. (b) MUSCL-4 scheme.

Fig. 18: Vorticity contours at the plane x/R= 1 of the blade 1 (ψ= 0) for the MUSCL-2 and MUSCL-4 schemes.

VI. Conclusions

This paper demonstrates the ability of HMB solver to accurately predict the rotor hover performance at low and high disc loadings with modest computer resources. The main conclusions are:

- Results of the steady flow around the XV-15 tiltrotor showed a better wake and higher resolution of the vortical structures when a higher-order scheme is used.
- The transition onset and distribution of skin friction are well predicted and, for this case, were found to have a mild effect on the overall figure of merit.

- The effect of the Mach number on the performance of the PSP blade is captured by CFD.
- The high-order scheme proposed was also able to compute the flow around the UH-60A rotor in forward flight.

Acknowledgements

The use of the cluster Chadwick of the University of Liverpool is gratefully acknowledged. Some results were obtained using the EPSRC funded ARCHIE-WeSt High Performance Computer (`www.archie-west.ac.uk`), EPSRC grant no. EP/K000586/1. Part of this work is funded under the HiperTilt Project of the UK Technology Strategy Board (TSB) and Leonardo Helicopters under Contract Nr. 101370. The authors also acknowledged the support of the UK VNL.

[1] Brocklehurst, A. and Barakos, G. N., "A Review of Helicopter Rotor Blade Tip Shapes," *Progress in Aerospace Sciences*, Vol. 56, No. 1, 2013, pp. 35–74, DOI: 10.1016/j.paerosci.2012.06.003.

[2] Johnson, W., *Helicopter Theory*, Princeton University Press, New Jersey, 1980.

[3] Balch, D. T., Saccullo, A., and Sheehy, T. W., "Experimental Study of Main Rotor/Tail Rotor/Airframe Interactions in Hover - Volume I," NASA CR–166485, June 1983.

[4] Balch, D. T., "Experimental Study of Main Rotor/Tail Rotor/Airframe Interactions in Hover," *Journal of the American Helicopter Society*, Vol. 30, No. 2, 1985, pp. 49–56, DOI:http://dx.doi.org/10.4050/JAHS.30.49.

[5] Balch, D. T. and Lombardi, J., "Experimental Study of Main Rotor Tip Geometry and Tail Rotor Interactions in Hover. Vol I - Text and Figures," NASA CR–177336, Feb. 1985.

[6] Balch, D. T. and Lombardi, J., "Experimental Study of Main Rotor Tip Geometry and Tail Rotor Interactions in Hover. Vol II - Run Log and Tabulated Data Progress Report," NASA CR–177336, Feb. 1985.

[7] "Advancement of Proprotor Technology, Task II - Wind-Tunnel Test Results," NASA CR–114363, Sept. 1971.

[8] Weiberg, J. A. and Maisel, M. D., "Wind-Tunnel Tests of the XV-15 Tilt Rotor Aircraft," NASA TM–81177, April 1980.

[9] Felker, F. F., Betzina, M. D., and Signor, D. B., "Performance and Loads Data from a Hover Test of a Full-Scale XV-15 Rotor," NASA TM–86833, Sept. 1985.

[10] Bartie, K., Alexander, H., McVeigh, M., Mon, S. L., and Bishop, H., "Hover Performance Tests of Baseline Meter and Advanced Technology Blade (ATB) Rotor Systems for the XV-15 Tilt Rotor Aircraft," NASA CR–114626, Oct. 1986.

[11] Light, J. S., "Results from an XV-15 Rotor Test in the National Full-Scale Aerodynamics Complex," *Proceedings of the 53rd American Helicopter Society Annual Forum*, AHS, Virginia Beach, Virginia, 1997.

[12] Betzina, M. D., "Rotor Performance of an Isolated Full-Scale XV-15 Tiltrotor in Helicopter Mode," *Proceedings of the American Helicopter Society Aerodynamics, Acoustics, and Test and Evaluation Technical Specialist Meeting*, AHS, San Francisco, CA, 2002, pp. 1–12.

[13] Wadcock, A. J., Yamauchi, G. K., and Driver, D. M., "Skin Friction Measurements on a Hovering Full-Scale Tilt Rotor," *Journal American Helicopter Society*, Vol. 99, No. 4, 1999, pp. 312–319.

[14] Wong, O. D., Noonan, K. W., Watkins, A. N., Jenkins, L. N., and Yao, C. S., "Non-Intrusive Measurements of a Four-Bladed Rotor in Hover - A First Look," *Proceedings of the American Helicopter Society Aeromechanics Specialists*, AHS-2010, San Francisco, California, 2010, pp. 1–11.

[15] Wong, O. D., Watkins, A. N., Goodman, K. Z., Crafton, J., Forlines, A., Goss, L., Gregory, J. W., and Juliano, T. J., "Blade Tip Pressure Measurements using Pressure Sensitive Paint," *Proceedings of the 68th American Helicopter Society*, AHS-2012-000233, Fort Worth, Texas, 2012, pp. 1–14.

[16] Overmeyer, A. D. and and, P. B. M., "Measured Boundary Layer Transition and Rotor Hover Performance at Model Scale," *Proceedings of the 55th Aerospace Sciences Meeting*, AIAA-2017-1872, Grapevine, Texas, 2017, pp. 1–36.

[17] Barakos, G., Steijl, R., Badcock, K., and Brocklehurst, A., "Development of CFD Capability for Full Helicopter Engineering Analysis," *Proceedings of the 31st European Rotorcraft Forum*, ERF, Florence, Italy, 2005, pp. 1–15.

[18] Lawson, S. J., Steijl, R., Woodgate, M., and Barakos, G. N., "High performance computing for challenging problems in computational fluid dynamics," *Progress in Aerospace Sciences 2012*, Vol. 52, No. 1, 2012, pp. 19–29, DOI: 10.1016/j.paerosci.2012.03.004.

[19] Steijl, R. and Barakos, G. N., "Sliding mesh algorithm for CFD analysis of helicopter rotor-fuselage aerodynamics," *International Journal for Numerical Methods in Fluids 2008*, Vol. 58, No. 5, 2008, pp. 527–549, DOI: 10.1002/d.1757.

[20] Steijl, R., Barakos, G. N., and Badcock, K., "A framework for CFD analysis of helicopter rotors in hover and forward flight," *International Journal for Numerical Methods in Fluids 2006*, Vol. 51, No. 8, 2006, pp. 819–847, DOI: 10.1002/d.1086.

[21] Hirt, C. W., Amsten, A. A., and Cook, J. L., "An Arbitrary Lagrangian-Eulerian Computing Method for All Flow Speeds," *Journal of Computational Physics*, Vol. 14, No. 3, 1974, pp. 227–253, DOI: 10.1016/0021-9991(74)90051-5.

[22] Osher, S. and Chakravarthy, S., "Upwind Schemes and Boundary Conditions with Applications to Euler Equations in General Geometries," *Journal of Computational Physics*, Vol. 50, No. 3, 1983, pp. 447–481, DOI: 10.1016/0021-9991(83)90106-7.

[23] Roe, P. L., "Approximate Riemann Solvers, Parameter Vectors, and Difference Schemes," *Journal of Computational Physics*, Vol. 43, No. 2, 1981, pp. 357–372, DOI: 10.1016/0021-9991(81)90128-5.

[24] van Leer, B., "Towards the Ultimate Conservative Difference Scheme. V. A Second-Order Sequel to Godunov's Method," *Journal of Computational Physics*, Vol. 32, No. 1, 1979, pp. 101–136, DOI: 10.1016/0021-9991(79)90145-1.

[25] van Albada, G. D., van Leer, B., and Roberts, W. W., "A Comparative Study of Computational Methods in Cosmic Gas Dynamics," *Astronomy and Astrophysics*, Vol. 108, No. 1, 1982, pp. 76–84.

[26] Axelsson, O., *Iterative Solution Methods*, Cambridge University Press, 1994.

[27] Burg, C. O. E., "Higher Order Variable Extrapolation For Unstructured Finite Volume RANS Flow Solvers," *Proceedings of the Seventieth AIAA Computational Fluid Dynamics Conference*, AIAA, Toronto, Ontario, 2005, pp. 1–17.

[28] Yang, H. Q., Chen, Z. J., Przekwas, A., and Dudley, J., "A high-order CFD method using successive differentiation," *Journal of Computational Physics*, Vol. 281, No. 1, 2015, pp. 690–707, DOI: 10.1016/j.jcp.2014.10.046.

[29] Yang, H. Q. and Harris, R. E., "Vertex-centered, high-order schemes for turbulent flows," *Proceedings of the Fifty-Fourth Aerospace Sciences Meeting*, AIAA, San Diego, California, 2016, pp. 1–24.

[30] Anderson, W. K., Thomas, J. L., and van Leer, B., "Comparison of Finite Volume Flux Vector Splittings for the Euler Equations," *AIAA Journal*, Vol. 24, No. 9, 1986, pp. 1453–1460, DOI: 10.2514/3.9465.

[31] Menter, F. R., "Two-Equation Eddy-Viscosity Turbulence Models for Engineering Applications," *AIAA Journal*, Vol. 32, No. 8, 1994, pp. 1598–1605, DOI: 10.2514/3.12149.

[32] Menter, F. R., Smirnov, P. E., Liu, T., and Avancha, R., "A One-Equation Local Correlation-Based Transition Model," *Flow Turbulence Combust*, Vol. 95, No. 4, 2015, pp. 583–619, DOI:10.1007/s10494-015-9622-4.

[33] Menter, F., Langrtry, R., Rikki, R., Suzen, S., Huang, P., and Volker, S., "A Correlation-Based Transition Model Using Local Variables - Part I: Model Formulation." *Journal of Turbomachinery*, Vol. 128, No. 3, 2006, pp. 1598–1605.

[34] Acree, C., "Rotor Design Options for Improving XV-15 Whirl-Flutter Stability Margins," NASA TP–2004-212262, March 2004.

[35] Maisel, M. D., Giulianetti, D. J., and Dugan, D. C., "The History of the XV-15 Tilt Rotor Research Aircraft: From Concept to Flight," NASA SP-2000-4517, 2000.

[36] Leishman, J. G., *Principles of Helicopter Aerodynamics*, Cambridge, 2000.

[37] Yoon, S., Pulliam, T. H., and Chaderjian, N. M., "Simulations of XV-15 Rotor Flows in Hover Using OVERFLOW," *Proceedings of the 50th AHS Aeromechanics Specialists*, AHS, San Francisco, CA, 2014, pp. 1–11.

[38] Ghosh, D., *Compact-Reconstruction Weighted Essentially Non-Oscillatory Schemes for Hyperbolic Conservation Laws*, Ph.D. thesis, University of Maryland, United States, Jan. 2013.

[39] Kocurek, J. D. and Tangler, J. L., "A Prescribed Wake Lifting Surface Hover Performance Analysis," *Journal of the American Helicopter Society*, Vol. 22, No. 1, 1977, pp. 24–35, DOI: 10.4050/JAHS.22.24.

[40] Landgrebe, A. J., "The Wake Geometry of a Hovering Rotor and its Influence on Rotor Performance," *Journal of the American Helicopter Society*, Vol. 17, No. 4, 1972, pp. 3–15, DOI: 10.4050/JAHS.17.3.

[41] Vieira, B. A. O., Kinzel, M. P., and Maughmer, M. D., "CFD Hover Predictions Including Boundary-Layer Transition," *Proceedings of the 55th Aerospace Sciences Meeting*, AIAA-2017-1665, Grapevine, Texas, 2017, pp. 1–16.

[42] Coder, J. G., "OVERFLOW Rotor Hover Simulations Using Advanced Turbulence and Transition Modeling," *Proceedings of the 55th Aerospace Sciences Meeting*, AIAA-2017-1432, Grapevine, Texas, 2017, pp. 1–19.

[43] Bousman, W. G., "Aerodynamic Characteristics of SC1095 and SC1094R8 Airfoils," NASA TP–2003-212265, Dec. 2003.

[44] Shinoda, P. M., Yeo, H., and Norman, T. R., "Rotor Performance of a UH-60 Rotor System in the NASA Ames 80-by 120-Foot Wind Tunnel," *Proceedings of 58th American Helicopter Society*, AHS, Montreal, Canada, 2002, pp. 1–18.

[45] Dindar, M., Shephard, M. S., Flaherty, J. E., and Jansen, K., "Adaptive CFD analysis for rotorcraft aerodynamics," *Computer Methods in Applied Mechanics and Engineering*, Vol. 189, No. 1, 2000, pp. 1055–1076, DOI: 10.1016/S0045-7825(99)00368-0.

[46] Kufeld, R., Balough, D., Cross, J., Studebaker, K., and Jennison, C., "Flight Testing the UH-60A Airloads Aircraft," *Proceedings of 50th American Helicopter Society*, AHS-50-1994-044, Alexandria, Virginia, 1994, pp. 1–22.